

# 3

## *On Synthesis, Optical and magnetic Properties of Semimagnetic Nanocrystals Growth in Glass Matrix*

Sidney Alves Lourenço<sup>1</sup>, Noelio Oliveira Dantas<sup>2</sup> and Ricardo Souza da Silva<sup>3</sup>

<sup>1</sup>Engenharia de Materiais, Universidade Tecnológica Federal do Paraná, 86036-370, Londrina, PR, Brazil

<sup>2</sup>Laboratório de Novos Materiais Isolantes e Semicondutores (LNMISS), Instituto de Física, Universidade Federal de Uberlândia, CP 593, CEP 38400-902, Uberlândia, Minas Gerais, Brazil

<sup>3</sup>Instituto de Ciências Exatas e Naturais e Educação (ICENE), Departamento de Física, Universidade Federal do Triângulo Mineiro, 38025-180, Uberaba, Minas Gerais, Brazil

### Outline:

Introduction.....	54
Synthesis of semimagnetic nanocrystals in glass environment.....	54
Synthesis of Pb <sub>1-x</sub> Mn <sub>x</sub> Se Nanocrystals.....	54
Synthesis of Pb <sub>1-x</sub> Co <sub>x</sub> Se Nanocrystals.....	55
Structural and Morphologic Properties of Semimagnetic Nanocrystals.....	55
X-Ray Diffraction and Magnetic Force Atomic of Pb <sub>1-x</sub> mnxse Nanocrystals.....	55
X-Ray Diffraction and Magnetic Force Atomic of Pb <sub>1-x</sub> ccoxse Nanocrystals.....	57
Magnetic Properties of Semimagnetic Nanocrystals.....	58
Electron Paramagnetic Resonance of Pb <sub>1-x</sub> mnxse Nanocrystals.....	58
Optical Properties of Semimagnetic Nanocrystals.....	60
Absorption and Photoluminescence of Pb <sub>1-x</sub> mnxse Nanocrystals.....	60
Absorption and Photoluminescence of Pb <sub>1-x</sub> ccoxse Nanocrystals.....	68
Conclusions.....	69
Acknowledgements .....	70
References.....	71

## Introduction

Substitutionally incorporated transition metal impurities into semiconductor nanocrystals (NCs) have opened possibility to development of new nanocrystalline materials as semimagnetic  $Pb_{1-x}Mn_xS$  [1,2],  $Pb_{1-x}Mn_xSe$  [3,4]  $Cd_{1-x}Mn_xS$ [5],  $Cd_{1-x}Co_xS$ [6] and  $Bi_{2-x}Mn_xS_3$ [7] NCs. The semimagnetic nanocrystal can be engineered to manipulate a small number of spins trapped in the hosting zero-dimension semiconductor structure, allowing for instance the onset of paramagnetism, ferromagnetism, antiferromagnetism or spin-glass behavior, depending on the impurity concentration and on the magnitude of the d–d (J) and sp–d ( $\alpha$ ,  $\beta$ ) exchange interactions between the magnetic impurity and the hosting crystal lattice[8–10]. Once set in the above-mentioned exchange interaction enables the control of both the magnetic and optical properties of the end material using external fields in regimes hardly achieved with other classes of materials. These structures are also good candidates for quantum computation, spin filters and quantum information, and other spintronic devices[11]. The investigations of PbSe semiconductor have attracted much attention due to the large exciton Bohr radius (46 nm) and the band-gap of  $E_{gPbSe} = 0.28$  eV, at room temperature [12]. By varying the material's doping profile (x), in  $Pb_{1-x}Mn_xSe$  and  $Pb_{1-x}Co_xSe$  semimagnetic, a fine tuning of the semiconductor band gap energy can be achieved. Furthermore, quantum size effects caused by shrinking bulk semimagnetic, as in nanoparticles, enhance the optical and the magnetic properties even further. As far as the physical properties are concerned undoped NCs are quite different from magnetic ion doped in NCs, as expected from the strong sp-d exchange coupling between the localized doping species and the carriers in the hosting NC band structure. The results of this chapter confirm the high quality of the semimagnetic  $Pb_{1-x}Mn_xSe$  and  $Pb_{1-x}Co_xSe$  NCs that were successfully grown by the fusion method. We report the synthesis process of nanocrystals in a glass matrix, the synthesis routes of semimagnetic nanocrystals grown in glass matrix and their investigation by experimental techniques of x-ray diffraction (XRD), atomic force microscope/magnetic force magnetic (AFM/MFM), optical absorption (OA) and photoluminescence (PL) investigations. We believe that this chapter can motivate further investigations and applications of other systems containing NCs.

## Synthesis of semimagnetic nanocrystals in glass environment

The advanced in chemical synthesis controlled of nanostructured materials providence a way of produce nanocrystals in function of size, shape and composition by various methodologies. In particular, a route of synthesis very attractive of semimagnetic NCs is obtained by fusion method in glass matrix with posterior thermal treatment, permitting the formation of NCs with excellent control and small dispersion of size [1-7]. We report the study of  $Pb_{1-x}Mn_xSe$  and  $Pb_{1-x}Co_xSe$  NCs synthesized in borosilicate glass matrix template using the fusion method.

### *Synthesis of $Pb_{1-x}Mn_xSe$ Nanocrystals*

Semimagnetic  $Pb_{1-x}Mn_xSe$  NCs were synthesized in a glass matrix (SNABP) with a nominal composition of  $40SiO_2 \cdot 30Na_2CO_3 \cdot 1Al_2O_3 \cdot 25B_2O_3 \cdot 4PbO$  (%mol) + 2[Se] (%wt), and Mn-doping concentration (x) varying with respect to Pb-content from 0 and 5%. The first step of sample preparation consisted of melting powder mixtures in an alumina crucible at 1200 °C for 30 minutes. Then, the crucible containing the melted mixture underwent quick cooling to room temperature. In the second step, thermal annealing of the previously melted glass matrix was carried out at 500 °C for different times in

order to enhance the diffusion of  $\text{Pb}^{2+}$ ,  $\text{Mn}^{2+}$ , and  $\text{Se}^{2-}$  species into the host matrix. As a result of the thermal annealing,  $\text{Pb}_{1-x}\text{Mn}_x\text{Se}$  NCs were formed in the glass template.

### ***Synthesis of $\text{Pb}_{1-x}\text{Co}_x\text{Se}$ Nanocrystals***

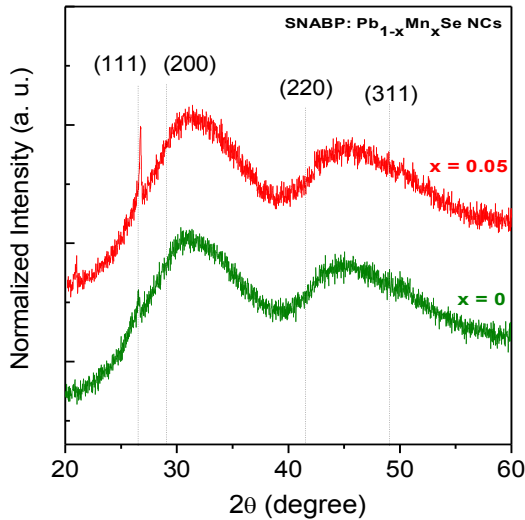
Semimagnetic  $\text{Pb}_{1-x}\text{Co}_x\text{Se}$  NCs were produced by the fusion method in the glass matrix with the following nominal composition:  $40\text{SiO}_2 \cdot 30\text{Na}_2\text{CO}_3 \cdot 1\text{Al}_2\text{O}_3 \cdot 25\text{B}_2\text{O}_3 \cdot 4\text{PbO}$  (%mol), herein quoted as SNABP glass matrix. The nominal composition of the nanocomposite was achieved by adding 2Se (%wt) plus  $x\text{Co}$  with respect to the  $(1-x)\text{Pb}$ , with  $x = 0$  and  $0.05$ . The samples were produced following two major preparation steps. In the first step the powder mixture was melted in an alumina crucible at  $1200^\circ\text{C}$  for 30 minutes, following a quick cooling of the crucible containing the melted mixture from  $1200^\circ\text{C}$  down to room-temperature. In the second step thermal annealing of the previously-melted glass matrix was carried out at  $500^\circ\text{C}$  for different times, with the purpose to enhance the diffusion of  $\text{Pb}^{2+}$ ,  $\text{Co}^{2+}$ , and  $\text{Se}^{2-}$  species within the hosting matrix. Due to the thermal annealing procedure  $\text{Pb}_{1-x}\text{Co}_x\text{Se}$  NCs were formed within the glass template.

## **Structural and Morphologic Properties of Semimagnetic Nanocrystals**

The structural and morphologic properties of  $\text{Pb}_{1-x}\text{Mn}_x\text{Se}$  and  $\text{Pb}_{1-x}\text{Co}_x\text{Se}$  nanocrystals were investigated by X-ray diffraction and Magnetic Force Atomic techniques.

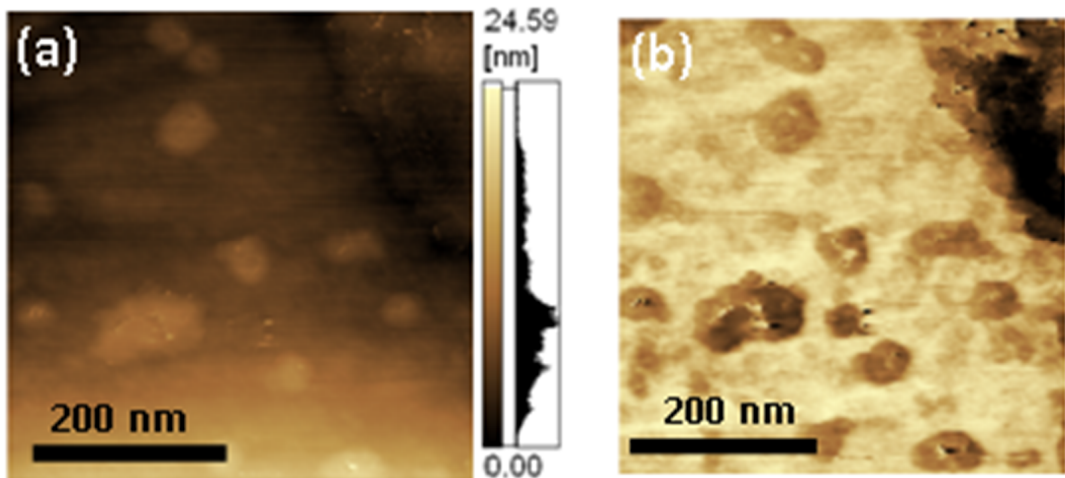
### ***X-Ray Diffraction and Magnetic Force Atomic of $\text{Pb}_{1-x}\text{Mn}_x\text{Se}$ Nanocrystals***

The XRD patterns of the SNABP:  $\text{Pb}_{1-x}\text{Mn}_x\text{Se}$  NCs samples for  $x = 0$  and  $x = 0.05$  are shown in Figure 3.1. It is noted that the typical PbSe rock salt crystal structure is preserved in the  $\text{Pb}_{1-x}\text{Mn}_x\text{Se}$  NCs. The XRD peaks (111), (200), (220) and (311) of NCs samples has been identified in the host amorphous glass matrix. Nevertheless, the characteristic XRD peaks shift towards lower diffraction angle values as the Mn-ion concentration in the hosting PbSe structure increases clearly indicating a change of the lattice constant. Nevertheless, the characteristic XRD peaks shift towards lower diffraction angle values as the Mn-ion concentration in the hosting PbSe structure decreases clearly indicating an increase of the lattice constant. Using the Vegard's law or rock salt PbSe and zincblende MnSe we performed the estimation of the lattice constant from the selected XRD peak (111). One found that the average lattice crystal constant of the  $x=0$  and  $0.05$   $\text{Pb}_{1-x}\text{Mn}_x\text{Se}$  NC samples  $6.130 \text{ \AA}$  and  $6.088 \text{ \AA}$ , respectively. This monotonic change observed in the lattice crystal constant is attributed to the replacement of the  $\text{Pb}^{2+}$ -ion, with larger ionic radius (119 pm) in the orthorhombic PbSe crystal structure, by  $\text{Mn}^{2+}$ -ion with smaller ionic radius (83 pm). By Mn-concentration to be very small, the crystalline structures for doped and undoped NCs are similar.

**FIGURE 3.1**

XRD measurements of PbSe ( $x=0$ ) and  $Pb_{0.95}Mn_{0.05}Se$  ( $x = 0.05$ ) NCs embedded in glass matrix. The effects associated to the incorporation of  $Mn^{2+}$  ions into PbSe NCs are seen as an intensity increase and a shift to higher  $2\theta$  diffraction angle of the (111) peak. Probably, the diffusion is enhanced along the (111) direction

Figure 3.2 presents the AFM/MFM images for the  $Pb_{0.95}Mn_{0.05}Se$  NCs samples subjected to the thermal annealing for 10 h, where we confirmed the high density of the nanocrystals with quantum confinement properties as well as bulk-like properties. AFM images for the  $Pb_{0.95}Mn_{0.05}Se$  NCs samples are shown in Figure 3.2(a). MFM images in Figure 3.2(b)

**FIGURE 3.2**

AFM/MFM images of  $Pb_{0.95}Mn_{0.05}Se$  NCs embedded in the glass matrix for average size of 6 nm. In (a) this influence is zero since the magnetic tip is lifted 24 nm from the sample; (b) the signal of the magnetic interactions is influenced by the sample topography in semimagnetic NCs

regarding magnetic phase, present some contrasts that correspond to magnetic nanocrystalline structures. This observation can be attributed to the fact that samples containing magnetic ions respond magnetically when induced by tip magnetization. Thus, the dark (light) contrasts shown in the AFM/MFM images, indicate that  $\text{Pb}_{0.95}\text{Mn}_{0.05}\text{Se}$  NCs are magnetic in a direction parallel (antiparallel) to tip magnetization. These results strongly indicate the formation of magnetized  $\text{Pb}_{0.95}\text{Mn}_{0.05}\text{Se}$  NCs in the SNABP glass matrix and the average size for  $\text{Pb}_{1-x}\text{Mn}_x\text{Se}$  NCs as 6 nm.

### ***X-Ray Diffraction and Magnetic Force Atomic of $\text{Pb}_{1-x}\text{Co}_x\text{Se}$ Nanocrystals***

The XRD patterns of the SNABP:  $\text{Pb}_{1-x}\text{Co}_x\text{Se}$  samples for  $x = 0$  and  $x = 0.10$  are shown in Figure 3.3. It is noted that the typical bulk PbSe rock salt crystal structure is preserved for the  $\text{Pb}_{1-x}\text{Co}_x\text{Se}$  dot samples observed the (111), (200), (220) and (311) peaks. Nevertheless, the characteristic XRD peaks is shifted towards lower diffraction angle values as the  $\text{Co}^{2+}$  incorporation in the hosting PbSe structure increases, and this is a clear indication that a decrease in the lattice constant is occurring. We have estimate the lattice constant of the structure using the (111), (200), (220) and (311) peaks of the XRD spectrum. Using the Vegard's law for rock salt PbSe and cubic  $\text{CoSe}_2$  crystal phases we performed the estimation of the lattice constant from the selected XRD peak (111) plane system change as the x-concentration. Here, the average lattice crystal constant found for  $\text{Pb}_{1-x}\text{Co}_x\text{Se}$  samples is 6.130 Å for  $x = 0.00$  (PbSe) and 6.103 Å for  $x = 0.10$  incorporation of  $\text{Co}^{2+}$  into the NCs. This monotonic decrease observed in the lattice constant can be attributed to the replacement of  $\text{Pb}^{2+}$ -ions, having larger ionic radius (119 pm) in the rock salt PbSe crystal structure, by  $\text{Co}^{2+}$ -ions with smaller ionic radius (75 pm). Once the grown samples have very small Co-concentration, the crystalline structures for undoped and doped NCs remained rock salt and showed similar values for the lattice constants.

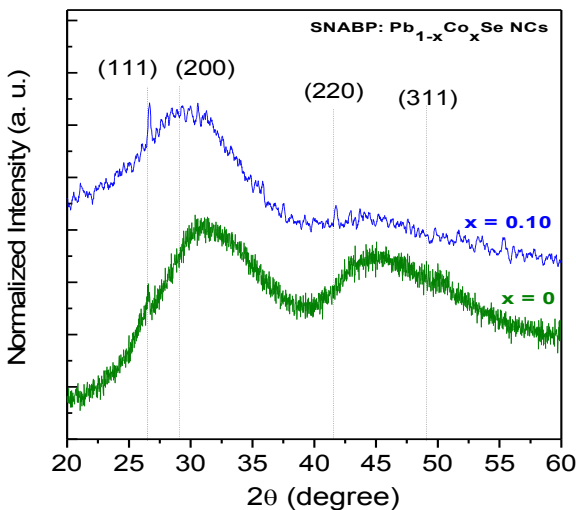


**FIGURE 3.3**

XRD measurements of PbSe and  $\text{Pb}_{0.90}\text{Co}_{0.10}\text{Se}$  NCs embedded in glass matrix

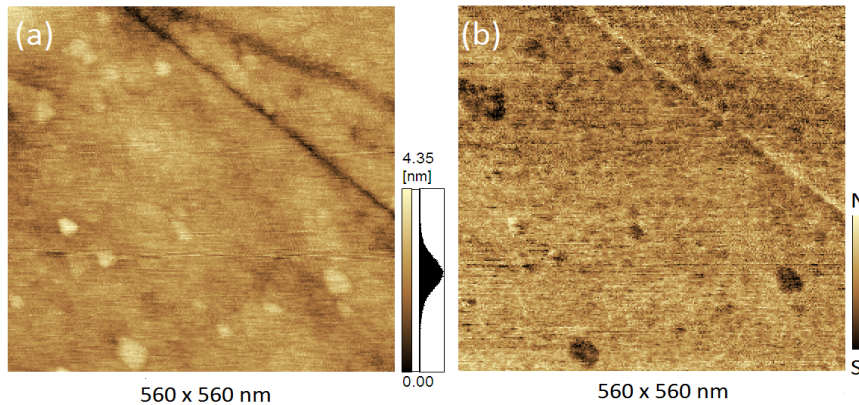


**FIGURE 3.4**

(a) Topographic MFM image showing a high amount of  $\text{Pb}_{0.90}\text{Co}_{0.10}\text{Se}$  NCs samples at sample's surface, and (b) the corresponding phase MFM image where the contrast between the South (S) and North (N) magnetic poles identifies the orientation of total magnetic moment of semimagnetic NCs

In addition, AFM/MFM images, represented in Figure 3.4, were measurements to the  $\text{Pb}_{0.90}\text{Co}_{0.10}\text{Se}$  NCs samples. The AFM image is also influenced by the sample topography, while in the MFM images there are only the magnetic interactions. The estimate average size for  $\text{Pb}_{0.90}\text{Co}_{0.10}\text{Se}$  NCs was 2.5 nm, in good agreement with average values obtained from calculation using k.p model for PbSe NCs[13]. In an attractive configuration, the NCs have magnetization in a parallel direction to the tip magnetization, resulting in dark areas of the MFM image. However, in a repulsive configuration, the NCs have magnetization in an antiparallel direction to the tip magnetization, resulting in bright areas of the MFM image. Therefore, the formation of the dark and bright fields related to a single spin domain in the  $\text{Pb}_{0.90}\text{Co}_{0.10}\text{Se}$  NCs is shown by the clear contrast in these MFM images. These results confirm the high quality of the synthesized  $\text{Pb}_{0.90}\text{Co}_{0.10}\text{Se}$  NCs which show a uniform distribution of total magnetic moments antiparallel to the tip magnetization direction.

## Magnetic Properties of Semimagnetic Nanocrystals

The magnetic properties of semimagnetic nanocrystals are influenced by exchange interactions sp-d between the electronic subsystems of magnetic ions with the NCs, changing the configuration of confined electronic states. The  $\text{Pb}_{1-x}\text{Mn}_x\text{Se}$  NCs were investigated by Electron Paramagnetic Resonance measurements.

### *Electron Paramagnetic Resonance of $\text{Pb}_{1-x}\text{Mn}_x\text{Se}$ Nanocrystals*

The crystal structure of the hosting PbSe has a strong influence into the incorporated  $\text{Mn}^{2+}$ -ions, as observed in the EPR spectrum recorded from glass sample embedded with  $\text{Pb}_{1-x}\text{Mn}_x\text{Se}$  NCs, favoring a strong electron spin-nucleus spin interaction. The experimental spectra of Mn-doped in NC samples can

be modeled by the spin Hamiltonian [1, 4]  $H = \hat{H}_z + \hat{H}_0$ , where  $H_z = \mu_e \hat{S} \cdot g_e \cdot \vec{B}$  is the Zeeman term with  $\mu_e$ ,  $g_e$ , and  $\vec{B}$  being the Bohr magneton, the Lande factor and the applied magnetic field, respectively.  $\hat{H}_0 = D[S_z^2 - S(S+1)/3] + E(S_x^2 - S_y^2) + A\hat{S} \cdot \hat{I}$ , in which the first two terms describe the zero-magnetic field fine-structure splitting due to spin-spin interaction of electrons, which is nonzero only in environments with symmetries lower than cubic, and the third term ( $A\hat{S} \cdot \hat{I}$ ) is stemmed from the hyperfine interaction between electron and nuclear spins. In a magnetic field the spin degeneracy of  $Mn^{2+}$ -ions will be lifted by the Zeeman splitting, resulting in six energy levels classified by magnetic electron spin quantum number  $M_S$ . Due to hyperfine splitting, each of these transitions will be split into six hyperfine levels characterized by the magnetic nuclear spin quantum number  $M_I$ . The main hyperfine lines in the spectra are due to allowed  $M_S = \pm 1$  transitions with  $\Delta M_I = 0$ , whereas other lines from forbidden transitions (due to breakdown of selection rule) with nonzero  $\Delta M_I$  may also be observed. Hence, the typical EPR of  $Mn^{2+}$  with electron ( $S = 5/2$ ) and nuclear ( $I = 5/2$ ) spins is composed of 30 lines – five fine structure transitions, each splitting into six hyperfine lines. The incorporation of metal-transition in NC sites cause changes in coordination states modifies the crystal field. These changes are analysed by EPR spectra. Typical EPR of  $Mn^{2+}$  with electron ( $S = 5/2$ ) and nuclear ( $I = 5/2$ ) spins is composed of 30 lines – five fine structure transitions, each splitting into six hyperfine lines. For the Mn-doped in PbSe NCs the hyperfine lines were only observed for the central  $M_S = 1/2 \leftrightarrow -1/2$  transition. The location of  $Mn^{2+}$  is presented in two different sites (surface and core) in NCs can be determinate by EPR measurements. In addition, the interaction constants A, D, and E depend strongly on the characteristics of the crystal field. For instance, when a  $Mn^{2+}$  ion is located close to or on the NC surface, a large structural difference between the NC and the glass matrix results in a larger hyperfine constant A and larger D and E values. Hence the EPR spectrum varies when the local structure of  $Mn^{2+}$  ion in the NC changes.

In Figure 3.5 are show the EPR spectra for the SNABP:  $Pb_{1-x}Mn_xSe$  and SNABP: x Mn, for  $x = 0.05$  samples synthesized by fusion method. The located of  $Mn^{2+}$  ions is induced for surface of PbSe NCs. The broad background signal observed in the EPR spectra is due to the electron spin-spin interaction of Mn-ions incorporated into the  $Pb_{1-x}Mn_xSe$  NCs structure. While the six-line structure confirms the uniform incorporation of  $Mn^{2+}$  ions in the hosting PbSe NCs structure the broad EPR line indicates the presence of exchange magnetic Mn-Mn interaction between Mn-ions agglomerated in small islands. The different between the glass samples SNABP:  $Pb_{1-x}Mn_xSe$  and SNABP: x Mn is observed in EPR spectra shows that the hyperfine interactions of  $Mn^{2+}$  ions is due the presence of PbSe NCs. The distance peak at peak of hyperfine structure for  $Pb_{1-x}Mn_xSe$  NCs is 9.3, 9.3, 7.8, 7.6 and 6.5 mT with average value of 8.1 mT. The hyperfine interactions observed for glass samples doped with  $Mn^{2+}$  are not evident as observed in presence of  $Pb_{1-x}Mn_xSe$  NCs and can be due the formation of small island of MnO in crystalline phase.

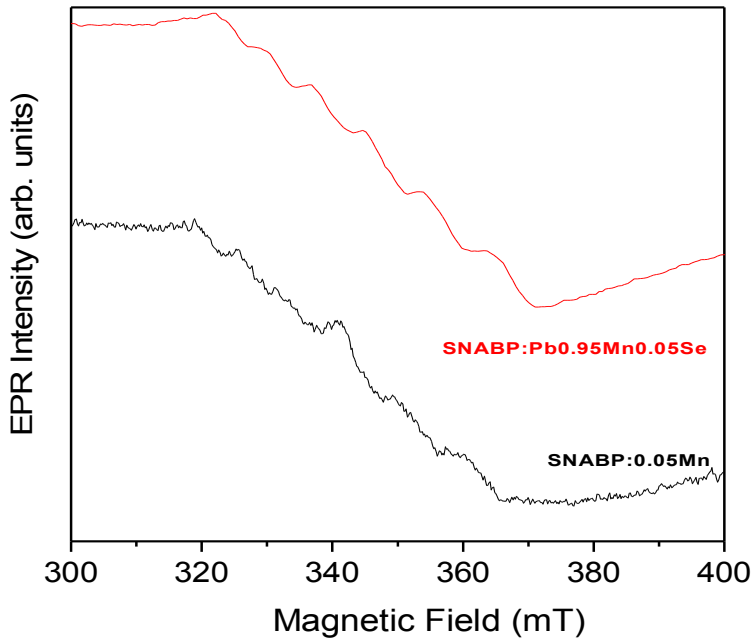


**FIGURE 3.5**

EPR spectra of glass matrix doped with  $x\text{Mn}$  and  $\text{Pb}_{1-x}\text{Mn}_x\text{Se}$  NCs for  $x = 0.05$

## Optical Properties of Semimagnetic Nanocrystals

The optical properties of semimagnetic nanocrystals  $\text{Pb}_{1-x}\text{Mn}_x\text{Se}$  and  $\text{Pb}_{1-x}\text{Co}_x\text{Se}$  embedded in glass matrix were investigated by Optical absorption and Photoluminescence techniques.

### *Absorption and Photoluminescence of $\text{Pb}_{1-x}\text{Mn}_x\text{Se}$ Nanocrystals*

Transition metal (TM) ion-doped II–VI or IV–VI semiconductors create new opportunities for optical applications. Recently, TM ion-doped chalcogenide semiconductor quantum dots (QDs) have attracted increasing attention because of their unique optical and electronic properties compared to their bulk counterparts that leads to high luminescence quantum efficiency, high optical gain with lower threshold [14–18]. Their optical and electronic properties, generally controlled as a function of QD size and shape, have applications in telecommunication [14], photovoltaic detectors [15], saturable absorbers for near-infrared passively mode-locked and Q-switched solid-state lasers [16], fluorescence biological labels [17], and cancer therapy [18]. Among these, diluted magnetic semiconductors (DMS) are expected to be key materials to future spintronic devices, because they possess charge and spin degrees of freedom in a single media with interesting magnetic, magneto-optical, magneto-electronic properties, among other [19–23].

From the viewpoint of the optical properties, TM ion-doped II–VI or IV–VI NCs can be classified in two regimes depending on the position of the energy level of the dopant ion in relation to the energy gap of the NC. These regimes define the photophysical and magneto-optical properties of NCs. In the first regime, named regime I, the energy level of the dopant ions is within the NC optical gap and in the regime II in the conduction band of the NC. Figure 3.6(a) shows a simplified comparison between band-gap energy of an II–VI or IV–VI semiconductor material and the energy of the  $\text{Mn}^{2+} {}^4\text{T}_1$  ligand-field excited state. For ZnS, ZnSe and CdS the  ${}^4\text{T}_1$  state is into the band gap energy (regime I) and for CdSe, CdTe, PbS, PbSe and PbTe the  ${}^4\text{T}_1$  state is into the conduction band of bulk semiconductors (regime II). In the first regime, after semiconductor excitation leads to rapid energy transfer ( $\sim 10^{-12}$  s) to the  $\text{Mn}^{2+}$  dopants, which leads to fluorescence with high quantum yields [24–28]. Thus, efficient energy transfer quenches excitonic emission and sensitizes the  $\text{Mn}^{2+}$  or  $\text{Co}^{2+}$  ligand-field dopant states, internal d-d transition with a slow decay (microseconds to milliseconds)[29,30]. In the regime II, the size-tunable emission and other attractive photophysical properties of undoped semiconductor QDs can be explored, while the TM ions introduce an additional degree of freedom to control these and other physical properties such as magnetic effects. In this scenario, encountered for narrow-gap semiconductor such as  $\text{Cd}_{1-x}\text{Mn}_x\text{Se}$ ,  $\text{Cd}_{1-x}\text{Mn}_x\text{Te}$ ,  $\text{Zn}_{1-x}\text{Mn}_x\text{Te}$  and  $\text{Pb}_{1-x}\text{Mn}_x\text{Se}$ , where the lowest excitonic states occur below all of the  $\text{Mn}^{2+}$  d-d

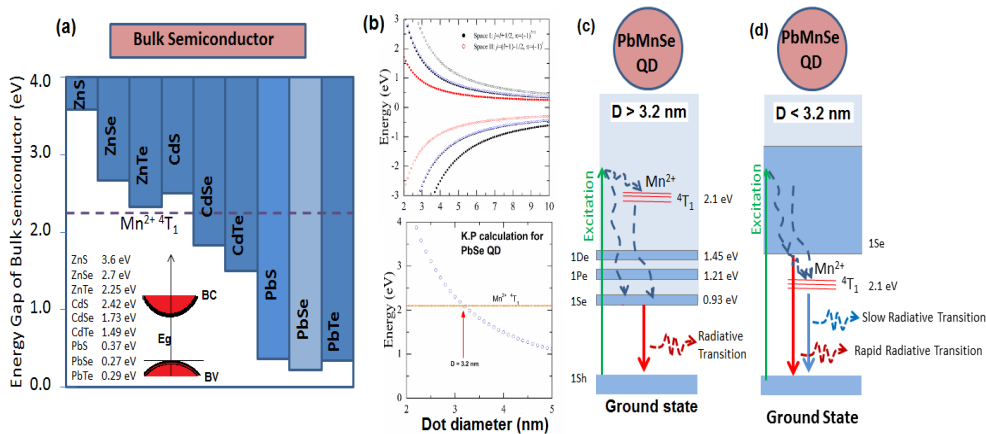


**FIGURE 3.6**

(a) Simplified comparison between the energy band-gaps of several II–VI and IV–VI semiconductor materials and the energy of the  $\text{Mn}^{2+} {}^4\text{T}_1$  ligand-field excited state. Figure 3.5.1(b) shows the energy calculation, using a K.P 4x4 method, as a function of PbSe QD size. Schematic representation of the recombination process in PbMnSe DMS QDs for diameter  $D > 3.2$  nm (Fig. c) and  $D < 3.2$  nm (Fig. d). Figure (d) shows a possible dual emission in PbMnSe QDs

excited states, alloys in the bulk form, the excitonic emission is not quenched by energy transfer to internal d-d excited states. The quantum size effect presented by QDs can change a material from regime II to regime I. More recently, a new relaxation scenario (regime III), for photoexcited  $\text{Mn}^{2+}$ -doped semiconductors was observed: small  $\text{Cd}_{1-x}\text{Mn}_x\text{Se}$  nanocrystals possessing electronic structures like that in scenario I exhibited excitonic luminescence like in scenario II[28]. This luminescence was characterized by extremely long excitonic PL decay times of up to  $\sim 15$   $\mu\text{s}$ , of magnitude longer than the intrinsic excitonic lifetimes. In this case, the slowly decaying  $\text{Mn}^{2+}$  excited state was shown to act as a population storage reservoir from which an excitonic population could be regenerated thermally,

showing tunable *dual* emission in doped semiconductor nanocrystals[28]. Energy calculations (K.P, 4x4 method [13], as a function of PbSe QD size, showed that the luminescence of the  ${}^4T_1 \rightarrow {}^6A_1$  state may occur at diameters smaller than 3.2 nm in PbMnSe QD systems, see figure 3.6b and 6d. Therefore, it is expected that very small lead-salt PbMnSe QDs may have  ${}^4T_1 \rightarrow {}^6A_1$  state luminescence resulting in the dual emission as that observed in colloidal ZnMnSe and CdMnSe Qds [28, 31] or CdMnSe and ZnMnTe QDs disperse throughout the glass template [32-34].

Figure 3.7 shows the room temperature optical absorption spectrum as a function of annealing time for (a) PbSe and (b)  $Pb_{0.95}Mn_{0.05}Se$  NCs embedded in glasses-SNABP. The annealed temperature was  $T = 500^\circ C$ . The spectra of the PbSe samples exhibit a single, pronounced peak whose intensity and position in energy are strongly dependent on annealing time. These shifts in optical features at low energy are due to longer annealing time and indicate increases in QD size [4]. At annealing time of 5 h there is more homogeneous size distribution of the PbSe NC, as can be seen by smaller line width of the OA spectra. Figures 3.7 (a) and 7(b) also show the OA spectra of the SNABP glass matrix. The structure in the near infrared spectral range (1350 nm) is related to the optical transition of the PbMnSe NCs [4]. Figure 3.7 shows that the undoped PbSe NCs and the  $Mn^{2+}$ -doped PbSe NCs exhibit confinement energy, indicated by the redshift of the OA band peak with increasing annealing time. Using the values of OA band peak and a confinement model based on effective mass approximation [13, 35], the average NC radius (R) was estimated. In this model the energy difference between electron and heavy

hole states, confined to a spherical region, is given by  $E_{conf} = E_g + \frac{\hbar^2 \pi^2}{2\mu R^2} - 1.8 \frac{e^2}{\epsilon R}$ , where R is the radius of the modeled spherical region,  $E_g$  is the energy gap of bulk semiconductor,  $\epsilon$  is the dielectric constant,  $\mu$  is the electron-heavy hole reduced effective mass and the third term is the electron-hole Coulomb interaction contribution[13,35]. For PbSe annealed for 3 h (R = 5.0 nm); 4 h (R = 5.4 nm); 5 h (R = 5.7 nm); 9 h (R = 6.2 nm); 12 h (R = 6.4 nm) and for  $Pb_{0.95}Mn_{0.05}Se$  annealed for 3 h (R = 5.7 nm); 4 h (R= 5.9 nm); 5 h (R= 6.0 nm) and for 10 h (R = 6.1nm).

Figure 3.7 (c) shows that the  $Mn^{2+}$  impurity affects nucleation dynamics. Here, the  $Mn^{2+}$ -doped sample causes a redshift after a short annealing period and a blueshift after a long annealing period compared to undoped PbSe NCs. A characteristic blueshift has been reported in the literature with increasing x in the band gap of  $Pb_{1-x}Mn_xSe$  NCs [4], in the  $Cd_{1-x}Mn_xS$  compared to undoped CdSe NCs[5], or in the  $Zn_{1-x}Mn_xSe$  Ncs[36]. The blueshift was observed between the OA peaks of PbSe and  $Pb_{0.95}Mn_{0.05}Se$  samples only after long thermal treatment times, see Figure 3.7 (c). The rapid saturation in the OA band peak observed, in this figure, as annealing time increases ( $Pb_{0.95}Mn_{0.05}Se$  NCs) is related to reduced  $Mn^{2+}$  concentration in the core of NCs, which reduces the **sp-d** interaction.

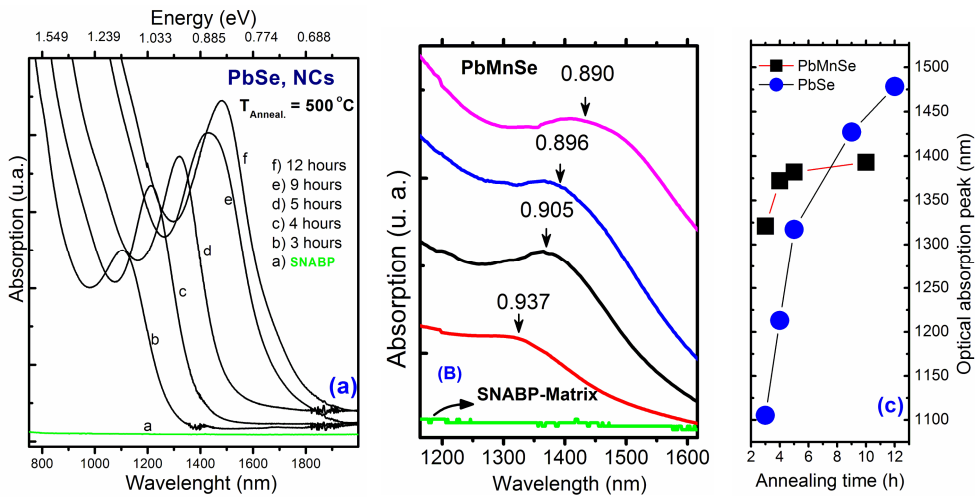


**FIGURE 3.7**

OA spectra of: (a) SNABP:PbSe and (b) semimagnetic SNABP: $\text{Pb}_{0.95}\text{Mn}_{0.05}\text{Se}$  NCs annealed for different time at 500 °C. (c) OA-peak as a function of annealing time for PbSe (blue circle) and  $\text{Pb}_{0.95}\text{Mn}_{0.05}\text{Se}$  NCs. [Ref.3]-

Reproduced by permission of the PCCP Owner Societies:  
<http://pubs.rsc.org/en/Content/ArticleLanding/2012/CP/c2cp40850c#!divAbstract>

Figure 3.8 presents PL spectra at 10 K of PbSe and  $\text{Pb}_{0.95}\text{Mn}_{0.05}\text{Se}$  NCs annealed at 500 °C for different times. An increase in annealing time leads to a redshift in the optical features of the PbSe and PbMnSe samples, similar to what happened with PbS NCs in a glass matrix [37]. For PbSe NCs, two types of dot families with different sizes and size dispersions were identified by spectral deconvolution in Gaussian components at 5 hours of annealing (blue-dashed lines and A' and B') and four types of dot families at 9 hours of annealing (red-dashed lines and A, B, C and D), (Figure 3.8 (a)). For  $\text{Pb}_{0.95}\text{Mn}_{0.05}\text{Se}$  NCs a smaller increase in annealing time leads to greater size dispersion of the dot family, which affects the position of PL peak energy. For both samples, FWHM of Gaussian components show that smaller dot families have greater size dispersion. In addition to redshift, increasing thermal treatment time due to quantum size effect, clearly reveals additional, larger families, (A and B in Figure 3.8 (a) and 3.8 (b)). Increases in NC size and the appearance of larger NCs contribute to the total redshift of the PL peak. Figures 7 and 8 show that samples with  $\text{Pb}_{1-x}\text{Mn}_x\text{Se}$  NCs, containing or not containing Mn ions and grown by fusion method, require different thermal treatment times for the nucleation of the same number of NC families. On the other hand, manganese incorporation modifies nucleation behavior, as previously observed in the OA spectra.

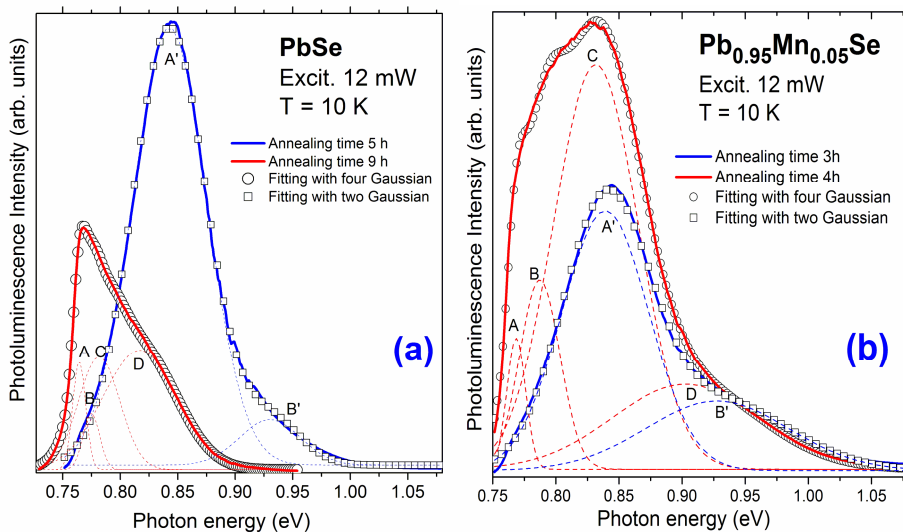


**FIGURE 3.8**

PL spectra of: (a) PbSe and (b)  $\text{Pb}_{0.95}\text{Mn}_{0.05}\text{Se}$  NCs at two different annealing times and at  $500^\circ\text{C}$ . The thick red and blue lines represent experimental data. Circles and squares represent convolution fittings of Gaussian components at 5 and 9 h (PbSe), and at 3 and 4 h ( $\text{Pb}_{0.95}\text{Mn}_{0.05}\text{Se}$ ), respectively. The thin dashed lines represent thin Gaussian components. [Ref.3]-Reproduced by permission of the PCCP Owner Societies:

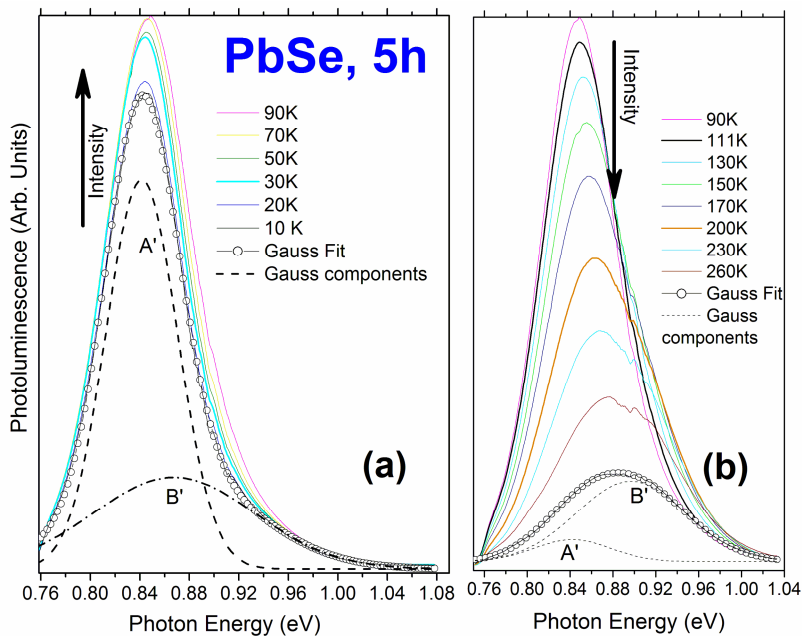
<http://pubs.rsc.org/en/Content/ArticleLanding/2012/CP/c2cp40850c#!divAbstract>

Figure 3.9 shows the PL spectra of PbSe annealed for 5 h (Figures (a) and (b)) and for 9 h (Figures (c) and (d)) as a function of temperature. At both treatment temperatures, the thermal evolution of the PL intensity appears "anomalous" compared to traditional III-V or II-VI semiconductor materials such as GaAs [38]. In other words, PL intensity generally decreases with increasing temperature [38]. In coupled quantum dot assemblies, generally the intensity of the PL spectra increases with temperature up to a certain temperature ( $T_k$ ). At higher temperatures, PL intensity decreases, as it does in traditional semiconductor materials.

The above mentioned PL results can be interpreted by considering the following processes: thermalization and state broadening in the NCs, thermally activated charge carrier transfer from intrinsic trapping states and energy transfer between different sized NCs. Trapping states may generally be present in glass containing NCs due to NC surface states and an intrinsic glass defect that acts as a carrier reservoir [39]. In strongly coupled quantum dot assemblies, electronic excitations can, in principle, delocalize across multiple dots. This leads to new states described by coherent superposition of individual dot wave functions that, as yet, are not well understood. In Figs. 9(a) and 9(c), the right side of PL spectra has a blueshift and the left side is almost constant in the 10–70 K range. These shifts are associated with carrier redistribution in the NC density states and energy transfer from surface states to dots. This can be seen in Figure 3.10 (b) where the PL intensity of both NC families increases until 70 K for samples annealed for 5 h. Both sides of the PL spectra have blueshifts at  $T > 70$ , leading to higher PL peak energy for type-A' and -B' NCs. This can be seen in Fig. 10(a), where -B' has a larger blueshift than -A'. Above 70 K, in addition to carrier redistribution in the NC states and carrier transfer from defect states, carrier transfer begins from type-A' to type-B' NCs. Above this temperature, type-A' PL intensity reduces considerably, whereas type-B' PL intensity continues to increase up to 170 K, (Fig. 10(b)). Thus, 70 K ( $K_B T \sim 6$  meV) activates the carrier transfer process from larger NC families to smaller

NC families and 170 K ( $K_B T \sim 15$  meV) is probably related to the escape of carriers from smaller NCs to nonradiative defect states.

Figures 3.11(a), (b) and (c) show the PL spectra at different temperatures for the  $\text{Pb}_{0.95}\text{Mn}_{0.05}\text{Se}$  sample annealed at 500 °C for 4 h. Similar to that observed in the PbSe NCs, Figs. (b) and (c) show that PL intensity of PbMnSe NCs increases up to temperature  $T_k$ . At higher temperatures, PL intensity decreases. For the PbMnSe NCs, annealed for 3 h,  $T_k$  is 80 K ( $K_B T = 6.89$  meV) and for 4 h  $T_k = 100$  K ( $K_B T = 8.61$  meV). Careful analysis of Fig. 11 shows that as the temperature increases, parts of the PL spectrum increase in intensity (B and C in Fig. 11 (b)) and other parts of the PL spectrum decrease in intensity (A and D in Fig. 11 (a)). These increases and decreases in the PL spectrum provide clear evidence of charge carrier thermal transfer between different sized NCs. The  $T_k$  values show that increases in annealing time raise the activation energy (potential barrier) needed to initiate carrier transfer between different sized NCs. These values also show that manganese ions decrease this barrier height.



**FIGURE 3.9**

PL spectra of PbSe annealed for 5 h ((a) and (b)) and 9 h ((c) and (d)) as a function of temperature. Circles represent convolution fittings of Gaussian components. The thin dashed lines, with peaks A' and B' (annealed for 5 h) and A, B, C, D (annealed for 9 h), represent the Gaussian components

[Ref. 3] - Reproduced by permission of the PCCP Owner Societies:

<http://pubs.rsc.org/en/Content/ArticleLanding/2012/CP/c2cp40850c#!divAbstract>

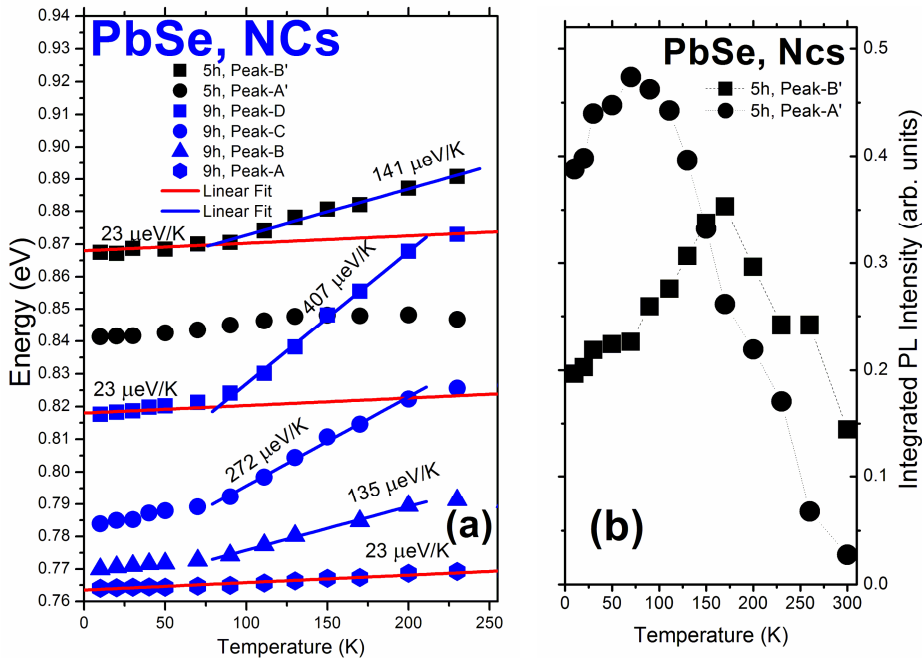


**FIGURE 3.10**

(a) PL peak energy as a function of temperature for PbSe NCs, (b) temperature dependence of the integrated PL intensity for PbSe NCs annealed for 5 h. The red and blue lines in (a) represent a linear fit.

[Ref.3]-Reproduced by permission of the PCCP Owner Societies:

<http://pubs.rsc.org/en/Content/ArticleLanding/2012/CP/c2cp40850c#!divAbstract>

These results for the  $\text{Mn}^{2+}$ -doped sample are in agreement with other analyses of the energy-dependent transfer rate of excitons from smaller to larger dots via electronic coupling [13, 40]. It has been predicted that further improvements in size selectivity, luminescence quantum yield, and well-controlled growth would enable highly efficient inter-dot energy transfer. For PbMnSe NCs annealed for 3 h, it can be seen that as the temperature increases (from  $T = 10$  K), carriers are thermally transferred from lower- to higher-energy states of the QD ensemble (type-B'). They then tunnel into a QD ensemble (type-A') through QD surface defect states or through the second energy level of a type-A' ensemble [40]. In this way, the quantity of carriers is reduced in the higher energy states of the type-B' ensemble leading to a reduction in radiative recombination in this spectral range. This shifts the peak-B' position to lower energies and reduces the FWHM value, (fig. 12(c)). On the other hand, the occupation of higher energy state of the QDs ensemble type-A' shifts the PL peak position to higher energy values and FWHM increases. In addition to the higher energy shift of the PL peak-A' with increasing temperature, due to carrier transfer, there is also a shift of the PL peak to higher energy due to the size- and temperature-dependence of the lowest energy state in the lead-salt QDs[41]. As annealing time increases, new families appear in the low spectral range energy. Fig. 8(b) shows that type-A' and type-B' QDs (PbMnSe annealed for 3 h) share important similarities with type-C and type-D QDs (PbMnSe annealed for 4 h), that is, these new families are type-A and type-B QDs. Actually, the PL peak energy of the type-D QDs redshifts

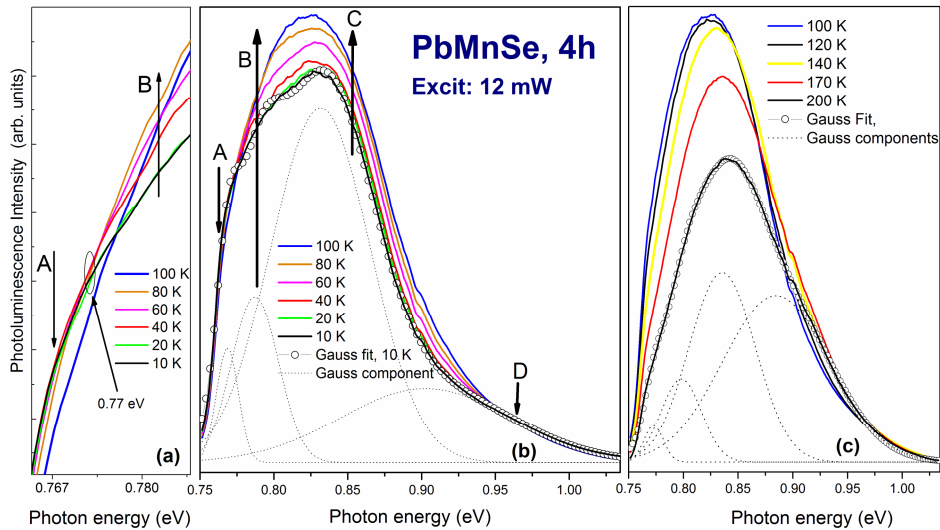


**FIGURE 3.11**

PL spectra of PbMnSe annealed for 4 h as a function of temperature. Thick lines represent experimental data and circles represent convolution fittings of Gaussian components of the sample at 10 K (b) and 200 K (c). Thin dashed lines with peaks at A, B, C and D, represent the Gaussian components

[Ref.3]- Reproduced by permission of the PCCP Owner Societies:

<http://pubs.rsc.org/en/Content/ArticleLanding/2012/CP/c2cp40850c#!divAbstract>

as temperature increases, similar to type-B'QDs, (Fig. 11(a)), and FWHM (Fig. 11(c)). FWHM of the type-C QDs increases up to 60 K and then decreases. This peak C behavior shows that above 60 K this QD family initiates carrier transfers to type-B QDs. This in turn, leads to additional line width increases for  $T > 60$  K, (Fig. 12 (d)). Thus, the  $\text{Mn}^{2+}$ -doped samples cause cascade carrier transfers from smaller QDs to larger QDs with increasing temperature. Increasing thermal annealing time allows for reorganization of the NCs into two new families, type-A and type-B. This leads to an increase in the energy level difference between neighboring QDs, which inhibits energy transfer between them.

In contrast to the sigmoid temperature dependence of the PL peak energy ( $E_{\text{PL}}(T)$ ) of type-D, type-C and type-B QDs, the  $E_{\text{PL}}(T)$  for type-A QDs, Fig. 12 (b), is linear. It is known that PbSe QDs have a temperature dependence of the excitonic transition energy with a positive coefficient for  $R > 3$  nm and a negative coefficient for  $R < 3$  nm [41]. After a linear fit, we obtained a coefficient of  $23 \mu\text{eV/K}$  for the  $\text{Pb}_{0.95}\text{Mn}_{0.05}\text{Se}$  system, which is consistent with values obtained for PbSe QDs with  $R = 5.9$  nm, Ref. [41]. It is also consistent with our experimental data presented in Figure 3.10(a) for PbSe NCs annealed for 9 h. Thus, we can see that the  $E_{\text{PL}}(T)$  of type-A QDs does not involve energy transfer from other families or from surface defects. Furthermore, due to low  $\text{Mn}^{2+}$  concentration, the  $\text{Pb}_{0.95}\text{Mn}_{0.05}\text{Se}$  system presents temperature dependence of excitonic transition energy similar to that of PbSe QDs. The low  $dE/dT$  coefficient obtained for PbSe NCs is linked to the high exciton Bohr radius,  $a_B = 46$  nm. Consequently, confinement is extreme in these QD's (e.g. this value is 8 times larger than it is for CdSe)[41]. It is well known that the optical properties of NPs can be significantly changed by interactions between nanostructures and their host material. This is mainly due to the formation of surface defects [42]. These surface defects are heavily dependent on NP size and become more significant with higher surface to volume ratios, which may lead to changes in vibrational mode, for example [43]. Thus, larger type-A QDs may have fewer surface defects and consequently lower energy

transfer from surface defects to NC states. Gradual reduction in the  $dE/dT$  coefficient, for  $70\text{ K} < T < 200\text{ K}$ , with increasing NC size, (PbSe system annealed for 9 h, Fig. 10(a)), provides additional evidence of carrier transfer reduction with increasing QD size.

However, the PbSe system annealed for 5 and 9 h demonstrates carrier transfer from larger QDs to smaller QDs, contrary to that observed in the PbMnSe system. This difference may be explained by increased coupling between PbMnSe NCs. The PbMnSe NCs have larger surface states than the PbSe NCs because surface  $\text{Mn}^{2+}$  ions produce the greatest number of defect states. This increases carrier transfer between PbMnSe NCs.

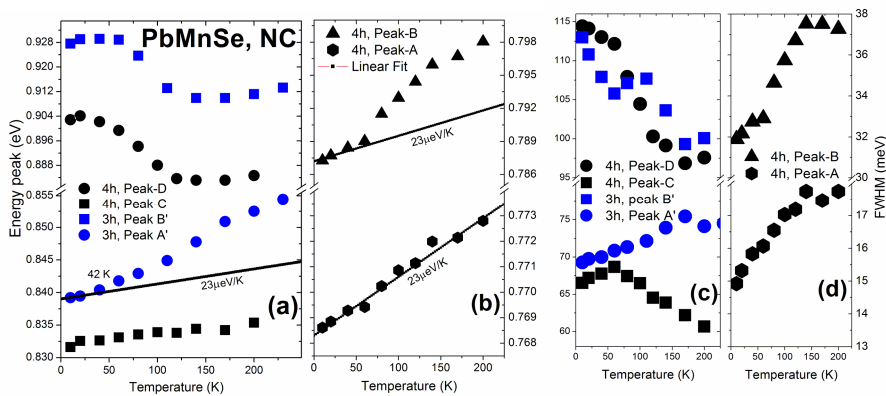


**FIGURE 3.12**

(a) and (b) show the PL peak energy as a function of temperature for PbMnSe NCs. In (c) and (d), it is showed the temperature dependence of FWHM. [Ref. 3] - Reproduced by permission of the PCCP Owner Societies: <http://pubs.rsc.org/en/Content/ArticleLanding/2012/CP/c2cp40850c#!divAbstract>

### Absorption and Photoluminescence of $\text{Pb}_{1-x}\text{Co}_x\text{Se}$ Nanocrystals

Cobalt doped materials attract the greatest interest in the last years.  $\text{Co}^{2+}$  doped YAG[44],  $\text{Co}^{2+}$  doped LaMgAlO [45],  $\text{Co}^{2+}$  doped MgAlO [46], and  $\text{Co}^{2+}$  doped ZnSe and ZnS [47,48] have been studied.  $\text{Co}^{2+}$  ( $^3d_7$ ) in ZnS, ZnSe, CdSe and others II-VI or IV-VI semiconductors substitute the cations ( $\text{Zn}^{2+}$ ,  $\text{Cd}^{2+}$ ,  $\text{Pb}^{2+}$ ) ions which are in tetrahedral sites. The tetrahedral site in the chalcogenides provides a higher oscillator strength for the  $3d-3d$  transitions. The energy-level diagram of  $\text{Co}^{2+}$  ( $^3d_7$ ) in tetrahedral sites is shown in inset of Figure 3.13. The ground level  $4F$  of a free ion  $\text{Co}^{2+}$  is split into three levels,  $^4T_1$ ,  $^4T_2$  and  $^4A_2$ , by the crystal field. In this materials, the broad absorption band at  $1300-2000\text{ nm}$  corresponds to  $^4A_2$  to  $^4T_1$  transition and that  $\sim 700\text{ nm}$  absorption band from  $^4F(^4A_2)$  to  $^4P(^4T_1)$  transition[49].

The long lifetime of  $^4F(^4A_2)$  states,  $290\text{ }\mu\text{s}$  for  $\text{Co}^{2+}:\text{ZnSe}$  NCs [50], make this an important new saturable absorber device for infrared lasers[45-49]. The luminescence properties of visible light-emitting  $\text{Co}^{2+}$ -doped QDs have been studied in the last years. There have, however, been few investigations of IR emission from of Co ion-doped chalcogenide QDs. Figure 3.13 shows optical absorption of  $\text{Co}^{2+}:\text{PbSe}$  NCs embedded in glass matrix. In the absorption spectra in visible light region (Fig. 13 (B)), a structure absorption band in the range from  $680$  to  $780\text{ nm}$  is observed, which is attributed to the spin and electric-dipole allowed  $^4A_2(F) \rightarrow ^4T_1(P)$   $\text{Co}^{2+}$  ligand-transition[50].

The near-infrared broad absorption band centered at  $1500\text{ nm}$  can be attributed to the spin and electric-dipole allowed  $^4A_2 \rightarrow ^4T_1(^4F)$  transition. This complicated structure of absorption bands has been

explained by the splitting of  ${}^4T_1({}^4P)$  and  ${}^4T_1({}^4F)$  levels in slightly distorted tetrahedral crystal field of oxygen environment around the  $\text{Co}^{2+}$  ions[49].

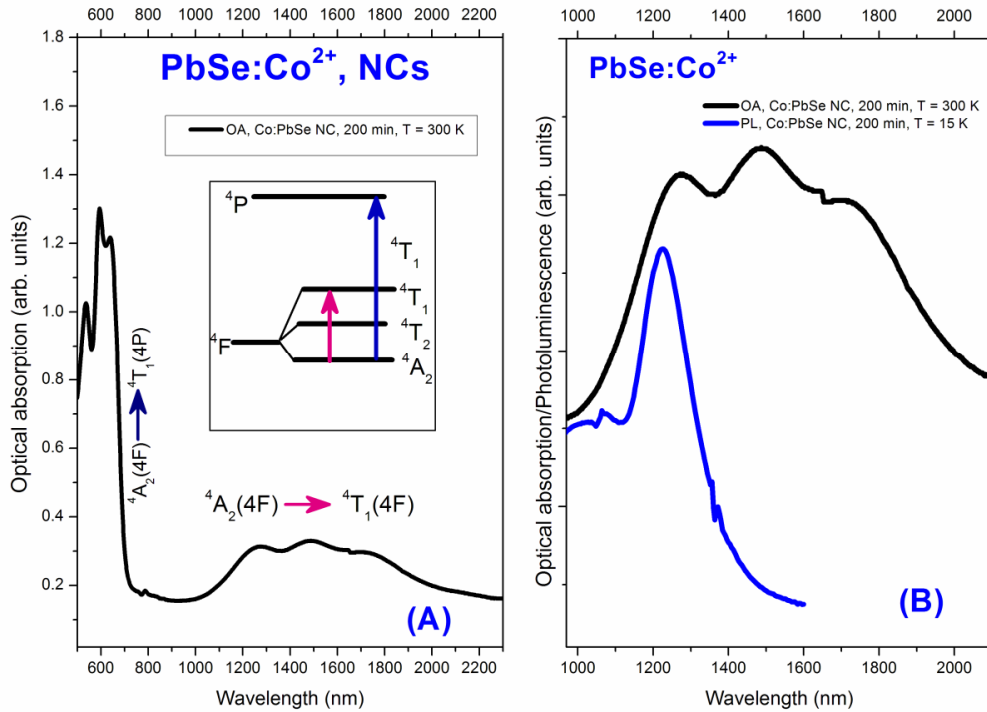


**FIGURE 3.13**

Room-temperature absorption spectra of  $\text{Co}^{2+}$ :PbSe NCs embedded in SNABP glass matrix annealed for 200 min,  $500^\circ\text{C}$ . Inset in Fig. A shows the energy level diagram of  $\text{Co}^{2+}$  ( $3d^7$ ) doped in tetrahedral host. Figure B shows the optical absorption at room and photoluminescence at low temperatures of  $\text{Co}^{2+}$ :PbSe NCs

The emission from  ${}^4T_2({}^4F)$  level to the ground  ${}^4A_2({}^4F)$  was observed in the range of 2.9 to 3.7  $\mu\text{m}$ [30,47,49]. The room temperature lifetime of the  $\text{Co}^{2+}$  ions in ZnSe was measured as 290  $\mu\text{s}$  [30]. Tsai et al.[49], have related that for low temperature emission lifetime of the  ${}^4T_2$  is 1170  $\mu\text{s}$  in ZnS and 1173  $\mu\text{s}$  in ZnSe, while at 300 K their lifetimes drops to 100–200  $\mu\text{s}$ . According to observation of Tsai et al.[49], and Burshtein et al. [51], the initially excited  ${}^4T_1({}^4F)$  state is assumed to decay nonradiatively and very fast to the lower  ${}^4T_2({}^4F)$  state. This picture is based on the fact that fluorescence from the  ${}^4T_1({}^4F)$  state has not been detected.

## Conclusions

In conclusions, we report the successfully synthesis of semimagnetic  $\text{Pb}_{1-x}\text{Mn}_x\text{Se}$  and  $\text{Pb}_{1-x}\text{Co}_x\text{Se}$  nanocrystals in glass matrix by fusion method. Our results confirm that the magnetic doping,  $\text{Mn}^{2+}$  and  $\text{Co}^{2+}$  ions localization, and quantum confinement play important roles on the magneto-optical properties of these NCs. The investigation of semimagnetic NCs provided by the experimental

techniques, showed that it was possible to control the optical, magnetic, and structural properties of these DMS NCs, confirming the high quality of the synthesized samples.

The temperature-dependent PL spectra show that the PL quenching temperature for different dot families is different and that the coupling between QDs plays a key role in the unusual temperature dependence of the PL spectra. Larger QDs have lower energy transfer, which can be explained by the dependence of the surface states on the NC surface to volume ratio. The coupling level between neighboring QD families apparently can cause energy transfer from lower to higher energy states or from higher to lower energy states. This coupling is affected by the dispersion and size of the QD families and in  $\text{Pb}_{1-x}\text{Mn}_x\text{Se}$  and  $\text{Pb}_{1-x}\text{Co}_x\text{Se}$  nanocrystals specific case by manganese doping and intrinsic glass defects. We believe that this chapter can motivate inspire further investigation of these systems in a search for possible device applications.

## Acknowledgements

The authors gratefully acknowledge the financial support from the Brazilian agencies: MCT/CNPq, Capes, Fapemig and Rede Mineira de Química (RQ-MG). We are also thankful for use of the facilities for the MFM measurements at the Instituto de Física (INFIS), Universidade Federal de Uberlândia (UFU), supported by a grant (Pró-Equipamentos) from the Brazilian Agency CAPES. We are also grateful to our collaborators: Anielle Christine Almeida Silva (UFU) by XRD measurements, Augusto Miguel Alcalde Milla (UFU) and Gilmar Eugenio Marques (UFSCAr) by k.p calculation, Felipe Chen Abrego (UFABC) and Oswaldo Baffa Filho (FFCLRP-USP) by EPR measurements.

## References

1. Silva R. S. Synthesis process controlled magnetic properties of  $\text{Pb}_{1-x}\text{Mn}_x\text{S}$  nanocrystals. *Applied Physics Letters* 2007; 90(25) 253114.
2. Dantas N. O. Control of magnetic behavior by  $\text{Pb}_{1-x}\text{Mn}_x\text{S}$  nanocrystals in a glass matrix. *Journal of Applied Physics* 2012; 111(6) 064311.
3. Lourenço S. A. Growth kinetic on the optical properties of the  $\text{Pb}_{1-x}\text{Mn}_x\text{Se}$  nanocrystals embedded in a glass matrix: thermal annealing and  $\text{Mn}^{2+}$  concentration. *Physical Chemistry Chemical Physics*. 2012; 14, 11040-11047.
4. Dantas N. O. Morphology in semimagnetic  $\text{Pb}_{1-x}\text{Mn}_x\text{Se}$  nanocrystals: Thermal annealing effects. *Applied Physics Letters* 2009; 94(26) 263103.
5. Dantas N. O. Evidence of  $\text{Cd}_{1-x}\text{Mn}_x\text{S}$  nanocrystal growth in a glass matrix by the fusion method. *Applied Physics Letters* 2008; 93(19)193115.
6. Neto E. S. F. Raman spectroscopy of very small  $\text{Cd}_{1-x}\text{Co}_x\text{S}$  quantum dots grown by a novel protocol: direct observation of acoustic-optical phonon coupling. *Journal of Raman Spectroscopy* 2013, 44, 1022-1032.
7. Panmand R. P. Novel and stable  $\text{Mn}^{2+}@\text{Bi}_2\text{S}_3$  quantum dots-glass system with giant magneto optical Faraday rotations. *Journal of Materials Chemistry C*. 2013; 1(6) 1203-1210.
8. Furdyna J. K. Diluted Magnetic Semiconductors. *Journal of Applied Physics*. 1988; 64(4) R29.
9. Ohno H. Making Nonmagnetic Semiconductors Ferromagnetic. *Science*. 1998; 281 (5379) 951-956.
10. Archer P I. Direct Observation of  $sp-d$  Exchange Interactions in Colloidal  $\text{Mn}^{2+}$  and  $\text{Co}^{2+}$  Doped  $\text{CdSe}$  Quantum Dots. *Nano letters* 2007, 7 (4) 1037–1043.
11. Žutić I, Petukhov A. Spintronics: Shedding light on nanomagnets. *Nature Nanotechnology* 2009; 4, 623 – 625.
12. Silva R S. Optical properties of IV-VI quantum dots embedded in glass: Size-effects. *Journal of Non-Crystalline Solids*. 2006; 352 (32-35) 3525-3529.
13. Silva R S. Optical properties of  $\text{PbSe}$  quantum dots embedded in oxide glass. *Journal of Non-Crystalline Solids*. 2006; 352 (32-35) 3522-3524.
14. Sukhovatkin V. Room-temperature amplified spontaneous emission at 1300 nm in solution-processed  $\text{PbS}$  quantum-dot films. *Optics Letters*. 2005; 30(2) 171-173.
15. Dissanayake M. D. M. N. A  $\text{PbS}$  nanocrystal- $\text{C}_{60}$  photovoltaic device for infrared light harvesting. *Applied Physics Letters*. 2007; 91(13) 133506.
16. Malyarevich A. M. Semiconductor-doped glass saturable absorbers for near-infrared solid-state lasers. *Journal of Applied Physics*. 2008; 103(8) 081301.
17. Jr M. B. Semiconductor Nanocrystals as Fluorescent Biological Labels. *Science*. 1998; 281(5385) 2013-2016.
18. Purushotham, Ramanujan R V. Modeling the performance of magnetic nanoparticles in multimodal cancer therapy. *Journal of Applied Physics*. 2010; 107(11) 114701.
19. Norris D. J. Doped Nanocrystals. *Science* 2008; 319(5871) 1776-1779.
20. Erwin A. C. Doping semiconductor nanocrystals. *Nature*. 2005; 436(7047) 91-94.
21. Nag A, Sarma D. D. White Light from  $\text{Mn}^{2+}$ -Doped  $\text{CdS}$  Nanocrystals: A New Approach. *Journal Physical Chemistry C*. 2007; 111(37) 13641-13644.
22. Han D. S. Synthesis and Magnetic Properties of Manganese-Doped  $\text{GaP}$  Nanowires. *Journal Physical Chemistry C*. 2005; 109(19) 9311-9316.
23. Beaulac R.  $\text{Mn}^{2+}$ -Doped  $\text{CdSe}$  Quantum Dots: New Inorganic Materials for Spin-Electronics and Spin-Photonics. *Advanced Functional Materials*. 2008; 18(24) 3873–3891.

24. Bol, A. A, Meijerink, A. Long-lived  $Mn^{2+}$  emission in nanocrystalline  $ZnS:Mn^{2+}$ . *Physical review B*. 1998; 58(24) R15997–R16000.
25. Suyver, J. F. Luminescence of nanocrystalline  $ZnSe:Mn^{2+}$ . *Physical Chemistry Chemical Physics*. 2000; 2(23) 5445–5448.
26. Norris D. J. High-Quality Manganese-Doped ZnSe Nanocrystals. *Nano Letters*. 2001; 1(1) 3–7.
27. Yang H. Photoluminescent and electroluminescent properties of Mn-doped ZnS nanocrystals. *Journal of Applied Physics*. 2003; 93(1) 586–592.
28. Vlaskin V. A. Tunable dual emission in doped semiconductor nanocrystals. *Nano Letters*. 2010; 10(9) 3670–3674.
29. Beaulac R., Ochsenein S. T., Gamelin D.R. Colloidal Transition Metal-Doped Quantum Dots. In: Klimov V. I., (ed.) *Nanocrystal Quantum Dots*. CRC Press: Boca Raton; 2010. P397–453.
30. DeLoach L. D. Transition metal-doped zinc chalcogenides: spectroscopy and laser demonstration of a new class of gain media. *IEEE Journal Quantum Electron*. 1996; 32(6) 885–895.
31. Beaulac R. Luminescence in colloidal  $Mn^{2+}$ -doped semiconductor nanocrystals. *Journal of Solid State Chemistry*. 2008; 181(7)1582–1589.
32. Neto E. S. F. N. Carrier dynamics in the luminescent states of  $Cd_{1-x}Mn_xS$  nanoparticles: effects of temperature and x-concentration. *Physical Chemistry Chemical Physics*. 2012; 14(4) 1493–1501.
33. Neto E. S. F. Magneto-optical properties of  $Cd_{1-x}Mn_xS$  nanoparticles: influences of magnetic doping,  $Mn^{2+}$  ions localization, and quantum confinement. *Physical Chemistry Chemical Physics*. 2012; 14(9) 3248–3255.
34. Dantas N. O. Thermal activated energy transfer between luminescent states of  $Mn^{2+}$ -doped ZnTe nanoparticles embedded in a glass matrix. *Physical Chemistry Chemical Physics*. 2012 14(10) 3520–3529.
35. Brus L. E. Electron–electron and electronhole interactions in small semiconductor crystallites: The size dependence of the lowest excited electronic state. *The Journal of Chemical Physics*. 1984; 80(9) 4403–4409.
36. Lad A. D. Magnetic behavior of manganese-doped ZnSe quantum dots. *Journal of Applied Physics*. 2007; 101(10) 103906.
37. Silva R. S. Synthesis and characterization of PbS quantum dots embedded in oxide glass. *Brazilian Journal of Physics*. 2006; 36(2a) 394–396.
38. Lourenço S. A. Temperature dependence of optical transitions in AlGaAs. *Journal of Applied Physics*. 2001; 89(10) 6159–6164.
39. Liu C. Temperature-dependent brightening and darkening of photoluminescence from PbS quantum dots in glasses. *Applied Physics Letters*. 2007; 90(24) 241111.
40. Lourenço S. A. Interdot carrier transfer in semimagnetic  $Pb_{1-x}Mn_xSe$  nanocrystals embedded in oxide glass. *Journal of Luminescence*. 2010; 130(11) 2118–2122.
41. Olkhovets A. Size-Dependent Temperature Variation of the Energy Gap in Lead-Salt Quantum Dots. *Physical Review Letters*. 1998; 81(16) 3539–3542.
42. Banyai IL, Koch S. W. *Semiconductor Quantum Dots*. World Scientific Publishing Co. 1993.
43. Neto E. S. F. N. Confirming the lattice contraction in CdSe nanocrystals grown in a glass matrix by Raman scattering. *Journal of Raman Spectroscopy*. 2010; 41(10) 1302–1305.
44. Camargo M. B.  $Co^{2+}:YSGG$  saturable absorber Q switch for infrared erbium lasers. *Optics Letters*. 1995; 20(3) 339–341.
45. Qi H. J.  $Co^{2+}:LaMgAl_{11}O_{19}$  saturable absorber Q-switch for a flash lamp pumped 1.54  $\mu m$  Er:glass laser. *Optics Express*. 2007; 15(6) 3195–3200.

46. Chen Y. J. Passive Q-switching of a diode-pumped 1520 nm Er:Yb:YAl<sub>3</sub>(BO<sub>3</sub>)<sub>4</sub> micro-laser with a Co<sup>2+</sup>:Mg<sub>0.4</sub>Al<sub>2.4</sub>O<sub>4</sub> saturable absorber. *Laser Physics Letters*. 2013; 10(9) 095803.
47. Jin-Jin Zhang. *Doping-induced emission of infrared light from Co<sup>2+</sup>-doped ZnSe quantum dots. Research on Chemical Intermediates*. 2011; 37, 383–388
48. Liu L. Optical properties of water-soluble Co<sup>2+</sup>:ZnS semiconductor nanocrystals synthesized by a hydrothermal process. *Materials Letters*. 2012; 66(1)121-124.
49. Tsai T. Y, Birnbaum M. Co<sup>2+</sup> : ZnS and Co<sup>2+</sup> : ZnSe saturable absorber Q switches. *Journal of Applied Physics*. 2000; 87(1) 25-29.
50. Feng S. Y. A cobalt-doped transparent glass ceramic saturable absorber Q-switch for a LD pumped Yb<sup>3+</sup>/Er<sup>3+</sup> glass microchip laser. *Laser Physics*. 2010; 10(8) 1687-1691.
51. Burshtein Z. Excited-state absorption at 1.57 μm in U<sup>2+</sup>:CaF<sub>2</sub> and Co<sup>2+</sup>:ZnSe saturable absorbers. *Optical Materials*. 2001; 15(4) 285-291.